

# Atmospheric turbulence characterization with the Keck adaptive optics systems. I. Open-loop data

Matthias Schöck, David Le Mignant, Gary A. Chanan, Peter L. Wizinowich, and Marcos A. van Dam

We present a detailed investigation of different methods of the characterization of atmospheric turbulence with the adaptive optics systems of the W. M. Keck Observatory. The main problems of such a characterization are the separation of instrumental and atmospheric effects and the accurate calibration of the devices involved. Therefore we mostly describe the practical issues of the analysis. We show that two methods, the analysis of differential image motion structure functions and the Zernike decomposition of the wave-front phase, produce values of the atmospheric coherence length  $r_0$  that are in excellent agreement with results from long-exposure images. The main error source is the calibration of the wave-front sensor. Values determined for the outer scale  $\mathcal{L}_0$  are consistent between the methods and with typical  $\mathcal{L}_0$  values found at other sites, that is, of the order of tens of meters. © 2003 Optical Society of America

OCIS codes: 010.1080, 010.1330, 010.7350.

## 1. Introduction

Adaptive optics (AO) systems have been implemented at many astronomical telescopes over the past 15 years, and most are now in or approaching routine operation.<sup>1–7</sup> In spite of constant improvements, however, AO systems frequently do not perform as desired, either in general or at particular times. A comparison between expected and actual performance can be performed only in a meaningful way if the turbulence conditions through which the telescope is observing are known. Unfortunately, this information is usually not readily available for most AO systems. However, AO systems are generally capable of recording telemetry data of both the measured wave-front distortions and the response of the AO system to these distortions. These telemetry data form, in principle, an ideal basis for analyzing the turbulence above the telescope. Many such at-

tempts have been made since the first AO systems went into operation (see, for example, Refs. 6, 8–13 and references therein), but to our knowledge there exists no AO system at which a comprehensive study of atmospheric conditions is routinely and automatically performed based on the output of the AO system itself. This is due to the practical difficulty of obtaining accurate quantitative measurements of turbulence parameters without compromising the performance of the AO system. Atmospheric and system effects are difficult to separate, in particular in an automated mode. Overcoming this difficulty is not only essential for an accurate assessment of the system performance, but it would also aid with a better understanding of the turbulence conditions above the site and, possibly, of atmospheric turbulence in general. For these reasons, we are developing an atmospheric characterization tool for the AO systems of the two 10-m telescopes of the W. M. Keck Observatory. In this paper we present a detailed description of the techniques used to analyze open-loop and tilt-tip- (TT-) loop-closed data and of the problems of such an analysis.

In Section 2 we introduce the types of data that are used for the analysis described in this paper. We also explain the conditioning needed for these data. Section 3 contains a detailed description of the wave-front sensor (WFS) calibration. We show that this calibration is one of the most important and most critical parts of the analysis. The two most reliable

---

M. Schöck (mschoeck@uci.edu) and G. A. Chanan are with the Department of Physics and Astronomy, 4129 Frederick Reines Hall, University of California, Irvine, Irvine, California 92697. D. Le Mignant and P. O. Wizinowich are with the W. M. Keck Observatory, 65-1120 Mamalahoa Highway, Kamuela, Hawaii 96743. M. A. van Dam is with the Lawrence Livermore National Laboratory, 7000 East Avenue, Livermore, California 94550.

Received 25 November 2002; revised manuscript received 6 March 2003.

0003-6935/03/193705-16\$15.00/0

© 2003 Optical Society of America

methods for the characterization of atmospheric turbulence, use of differential image motion (DIM) structure functions and the decomposition of the wave-front phase into Zernike modes, are described in Sections 4 and 5. We briefly touch on the temporal analysis of the data in Section 6. Sample results obtained with the atmospheric characterization tool are given in Section 7, and conclusions are provided in Section 8.

## 2. Data

### A. Open-Loop and Tilt-Tip-Loop-Closed Data

The Keck AO systems, like most other AO systems, have a separate TT loop and deformable mirror (DM) loop. If the DM loop is open, we refer to the data taken as open-loop data (TT and DM loop open) and TT-loop-closed data (TT loop closed, DM loop open). In both cases, the data of interest are the WFS measurements. If both loops are closed, we require both the WFS measurement and the DM position telemetry data. The main problem with the open-loop and TT-loop-closed analysis is the calibration of the data, in particular the strong dependence of the calibration on the spot size on the WFS detector. The problem with closed-loop data is the existence of dynamical system contributions to the telemetry data that cannot easily be separated from atmospheric contributions. We defer a discussion of closed-loop data to a future publication.

The Keck AO systems use CCD-based Shack-Hartmann WFSs consisting of quadrant cells. The dynamic range of the distortions measured by each subaperture is so large for open-loop data that these WFSs work in a strongly nonlinear and partially saturated regime as we describe in detail in Subsection 3.C. If, on the other hand, the TT loop is closed, the wave-front distortions measured by the WFS are small and the WFS operates in the linear or close-to-linear regime. Although the data are contaminated by the varying and not always well-understood residual global tilt, this does not matter because the data are already contaminated by apparent global tilts of the wave front caused by telescope vibrations and tracking errors. Only methods that are independent of the overall tilt of the wave front can be used, in any case, and the introduction of an additional tilt error—or the removal of the majority of the tilt by the TT mirror—has no effect on the results. We therefore never analyze open-loop data, but always have at least the TT loop closed.

We refer to the data analyzed in this paper as either diagnostics or telemetry data. Diagnostic data can be taken at the full frame rate of the Keck AO WFS (up to 672 Hz for bright guide stars) but cannot contain more than 1000 frames (1.5 s of data at 672 Hz). Telemetry data can be a time series of arbitrary lengths but they are taken at a much lower (of the order of a few hertz) and nonconstant frame rate. For both diagnostics and telemetry data, the exposure time of the individual sample is the inverse of the system frame rate and can be considered es-

entially instantaneous. The Keck WFSs have  $20 \times 20$  subapertures, 241 of which are fully illuminated at any time. See Refs. 7 and 14 for detailed descriptions of the Keck AO systems and Ref. 15 for an example of the relationship between the subapertures and the 36 primary mirror segments. In TT-loop-closed operation, the only data necessary are the centroids measured by the WFS. Because the accurate calibration of these centroids is critically important for obtaining quantitative results, we have put significant effort into this calibration. It is described in detail in Section 3.

### B. Data Conditioning

Before the data can be analyzed, a small amount of conditioning is necessary. First, because of the hexagonal shape of the Keck pupil and the secondary mirror obscuration, the pattern of illuminated subapertures on the WFS is not always the same. For obvious reasons, the nonilluminated subapertures have to be excluded from the data. Second, because only the time-varying wave-front distortions are caused by atmospheric turbulence, static wave-front aberrations have to be removed. This is done simply by calculating the time average of the WFS measurements over the entire data set and removing this average from each frame. This removal, however, gives rise to an additional complication for diagnostics data because 1.5 s is not sufficiently long for atmospheric turbulence to go through a statistically representative set of wave fronts for a 10-m aperture. Thus, subtracting the average removes not only the static aberrations, but also a significant amount of turbulence power from the data.

Telemetry data, which can span from a few seconds to several minutes, are preferable for the determination of quantities such as the atmospheric coherence length  $r_0$  and the outer scale of turbulence  $\mathcal{L}_0$ , which do not require a fast time series. However, because of the low and nonconstant frequency at which telemetry data are taken at Keck, these data cannot be used for temporal analyses such as the determination of the atmospheric coherence time  $\tau_0$  and of the temporal power spectra. For the temporal analysis, we require diagnostics data. The ideal setup is to take consecutive sets of telemetry and diagnostics data. The telemetry data are used to determine  $r_0$ ,  $\mathcal{L}_0$ , and similar quantities as well as the static aberrations of the wave front. These static aberrations are subtracted also from the diagnostics data that then are used for the temporal analysis of the wave front. Even so, the results from several diagnostics data sets should still be averaged—noting that  $r_0$  and  $\tau_0$  themselves do not need to be averaged but that their  $-5/3$  powers need to be averaged—because a 1.5-s set of turbulence measurements is not statistically representative of the turbulence conditions.

## 3. Wave-Front Sensor Calibration

To obtain reliable results from TT-loop-closed data, we require a quantitative calibration of the Keck

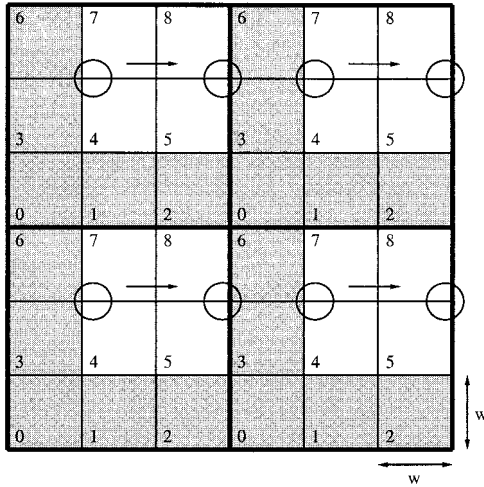


Fig. 1. Representation of the fiber spot moving across the pixels of Keck WFS subapertures. Shown in white are the pixels of four adjacent quadrant cells. The pixels of the guard rail in between the quadrant cells are shown in gray. The range of motion shown is approximately the maximum range over which the spot can be moved without vignetting. The parameter  $w$  of Eq. (1), corresponding to the linear pixel size, is also indicated.

WFSs. The WFS calibration is difficult in that the measured centroids depend on the spot size on the WFS detector. This spot size is not easily accessible as each subaperture is a quadrant detector. In addition, it changes with the seeing when one observes astronomical objects. In the following subsections we describe in detail the calibration process and its effect on the data analysis.

#### A. Spot Size

To measure the spot size of the image on the WFS detector, we used calibration fibers that can be placed in the focal planes of the Keck telescopes. The fibers were moved in the focal plane in a direction such that the resultant motion on the WFS CCD was parallel to the  $x$  direction on the CCD. In the perpendicular ( $y$ ) direction, the spots on each subaperture were aligned in the center of the quadrant cell. The situation is illustrated in Fig. 1, where the pixels of four adjacent subapertures are shown together with the rows of guard-rail pixels in between the subapertures. The same analysis for motion in the  $y$  direction was also performed, but is not presented here.

The intensity measured by pixels 4 and 7 in Fig. 1, averaged over all subapertures and after correction for fiber source intensity fluctuations, is shown as asterisks in Fig. 2. The intensity seen by pixels 5 and 8 is shown as diamonds. The shape of the curve is the convolution of the one-dimensional spot shape in the direction of the fiber motion,  $s(x)$ , and the individual pixel aperture function,

$$p(x) = \begin{cases} 1/w & -w/2 \leq x \leq w/2 \\ 0 & \text{otherwise.} \end{cases} \quad (1)$$

Here we assume that the pixel function is rectangular and of width  $w$ . The widening of the effective pixel

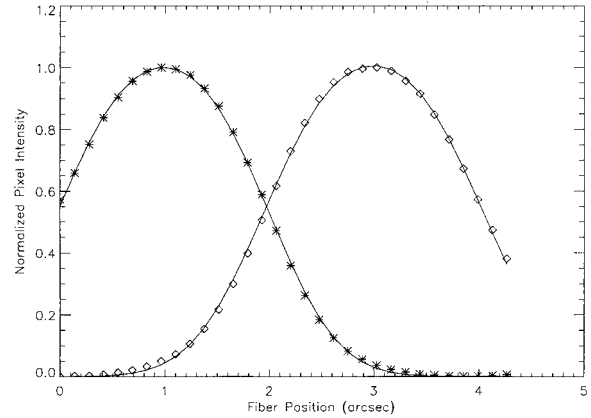


Fig. 2. Calibration of the spot size on the WFS. The asterisks and diamonds show the experimentally determined intensity on a pixel (averaged over all like pixels). The solid curves are the best-fit theoretical curves corresponding to these data.

width caused by CCD charge diffusion is included in the spot function  $s(x)$ . If we assume a Gaussian spot of variance  $\sigma^2$ ,

$$s(x) = \frac{1}{\sqrt{2\pi}\sigma} \exp\left(-\frac{x^2}{2\sigma^2}\right), \quad (2)$$

it is easy to show that the convolution is given by

$$\begin{aligned} i(x) &= s(x) * p(x) \\ &= \frac{1}{2w} \left\{ \operatorname{erf}\left[\frac{1}{\sqrt{2}\sigma} \left(x + \frac{w}{2}\right)\right] \right. \\ &\quad \left. - \operatorname{erf}\left[\frac{1}{\sqrt{2}\sigma} \left(x - \frac{w}{2}\right)\right] \right\}, \end{aligned} \quad (3)$$

where  $\operatorname{erf}(x)$  is the error function

$$\operatorname{erf}(x) = \frac{2}{\sqrt{\pi}} \int_0^x \exp(-t^2) dt. \quad (4)$$

The results of four-parameter ( $w$ ,  $\sigma$ , offset along the  $x$  axis, and overall scaling constant) fits of  $i(x)$  to the data are shown in Fig. 2 as solid curves. We obtain an excellent agreement between experiment and theory. In the example shown here, a small fiber, which can be considered a point source, was used with the Keck II AO system. We find  $w = 2.06$  arcsec and a full width at half-maximum (FWHM)  $\text{FWHM}_{\text{calib}} = 1.26$  arcsec for the Gaussian (that is,  $\sigma = 0.54$  arcsec). Although these values are reproducible with high accuracy at a given time, there seem to exist nightly variations of the spot size with a peak-to-value variation of almost 0.1 arcsec. The most common value for  $\text{FWHM}_{\text{calib}}$  is 1.29 arcsec, with the highest value found to date being 1.35 arcsec. Therefore the spot size should be calibrated frequently, and the most recent estimate for  $\sigma$  and  $w$  has to be used.

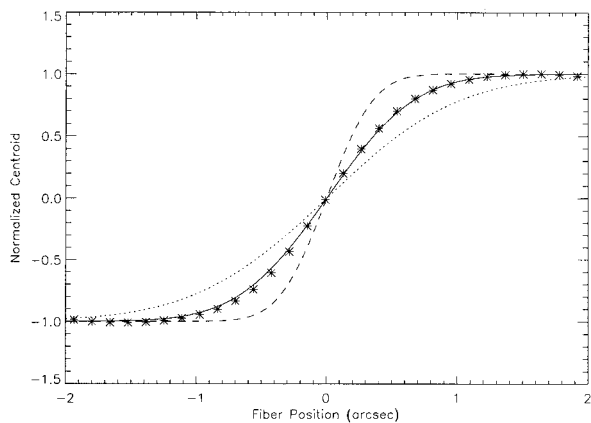


Fig. 3. Plot of centroids as measured by the Keck II WFS. Asterisks are the experimental data; the solid curve is the theoretical shape obtained by use of the values for spot size and pixel width that were determined by the fit shown in Fig. 2. The dotted curve is the theoretical curve for a spot size 0.25 arcsec larger than the best-fit value, and the dashed curve is for a spot size 0.25 arcsec smaller than the best-fit value.

### B. Centroids

We denote by  $I_i$  the intensity measured by pixel  $i$  in Fig. 1. The  $x$  centroid measured by the quadrant cell is given by

$$c_x = \frac{I_5 + I_8 - (I_4 + I_7)}{I_4 + I_5 + I_7 + I_8}. \quad (5)$$

If we again assume that the spot shape is Gaussian with an  $x$  cross section,  $s(x)$ , as given by Eq. (2), we can show that

$$I_4 + I_7 \propto \operatorname{erf}\left(\frac{x}{\sqrt{2}\sigma}\right) - \operatorname{erf}\left(\frac{x-w}{\sqrt{2}\sigma}\right), \quad (6)$$

$$I_5 + I_8 \propto \operatorname{erf}\left(\frac{x+w}{\sqrt{2}\sigma}\right) - \operatorname{erf}\left(\frac{x}{\sqrt{2}\sigma}\right). \quad (7)$$

We thus have an analytical equation

$$c_x = \frac{\operatorname{erf}\left(\frac{x+w}{\sqrt{2}\sigma}\right) - 2 \operatorname{erf}\left(\frac{x}{\sqrt{2}\sigma}\right) + \operatorname{erf}\left(\frac{x-w}{\sqrt{2}\sigma}\right)}{\operatorname{erf}\left(\frac{x+w}{\sqrt{2}\sigma}\right) - \operatorname{erf}\left(\frac{x-w}{\sqrt{2}\sigma}\right)} \quad (8)$$

describing the centroids measured by the WFS and can compare this equation with the measured centroids that were taken simultaneously with the spot-size calibration data. In Fig. 3 we show as asterisks the measured centroids, normalized to unity at the maximum to account for light leaking in from neighboring subapertures. The theoretical curve is shown as the solid curve. Note that this is not a best-fit theoretical curve, but is the theoretical curve obtained by use of the values for  $w$  and  $\sigma$  as found from the spot-size calibration. The agreement between data and theory is a verification of the spot-size results from Subsection 3.A, with the slight discrep-

ancies originating from leakage of light from neighboring subapertures. The dashed and dotted curves signify the theoretical curves for the cases when the spot size differs by 0.25 arcsec from 1.26 arcsec.

### C. Angle of Arrival Reconstruction

The conversion from measured centroids to the angle of arrival (AA) of the wave front is usually done simply by multiplying the centroids by a constant. This is certainly justified in closed-loop operation, in which case one almost exclusively encounters small centroid values and works in the linear regime of the curves in Fig. 3. For open-loop and TT-loop-closed data, however, one does not always work in the linear case as we demonstrate below, and this kind of conversion is an approximation. In the linear conversion approximation, the multiplicative conversion factor from centroids to AA,  $C_{\text{cent} \rightarrow \text{AA}}$ , is given by the inverse of the slope at the origin of the curve in Fig. 3:

$$C_{\text{cent} \rightarrow \text{AA}} = \sqrt{\frac{\pi}{2}} \sigma \frac{\operatorname{erf}\left(\frac{w}{\sqrt{2}\sigma}\right)}{1 - \exp\left(-\frac{w^2}{2\sigma^2}\right)}. \quad (9)$$

If this approximation is not sufficiently accurate, the only solution is the numerical inversion of the curve in Fig. 3, that is, of Eq. (8). In the following paragraphs we discuss whether the approximative method can be used with our data or if the curve inversion method is necessary. In the process of this discussion it will become apparent why TT-loop-closed data are preferable over open-loop data for the analysis of quadrant cell WFS data.

An example of the frequency of occurrence of AA values for a set of 1000 frames of open-loop diagnostics data is shown in Fig. 4. Figure 4(a) shows histograms of the measured centroids ( $x$  centroids are on the left;  $y$  centroids are offset by 2 units to the right) as the solid curves. As a reference, we also show the best-fit Gaussians to the histograms as dotted curves. Note that the static aberration removal as described in Subsection 2.B was not performed. The offsets of the two curves from the origin are predominantly due to pointing and tracking errors in open-loop operation. We can clearly see two effects of the nonlinearity of the quadrant detector in the curves that should be symmetrical, approximately Gaussian, and of equal width. First, both curves are nonsymmetrical, being steeper on the side of high centroid values. Second, the  $x$  centroids, taking on larger values on average than the  $y$  centroids, form a histogram with a much reduced width with respect to the  $y$  centroids. Obviously, the shapes of the curves do not change if a constant conversion factor is used to retrieve the AA as shown in Fig. 4(b). Open-loop data therefore are clearly not usable with the linear conversion approximation.

We can instead use the inversion of the centroid-AA relation to attempt the reconstruction of the original wave-front AA from open-loop data.

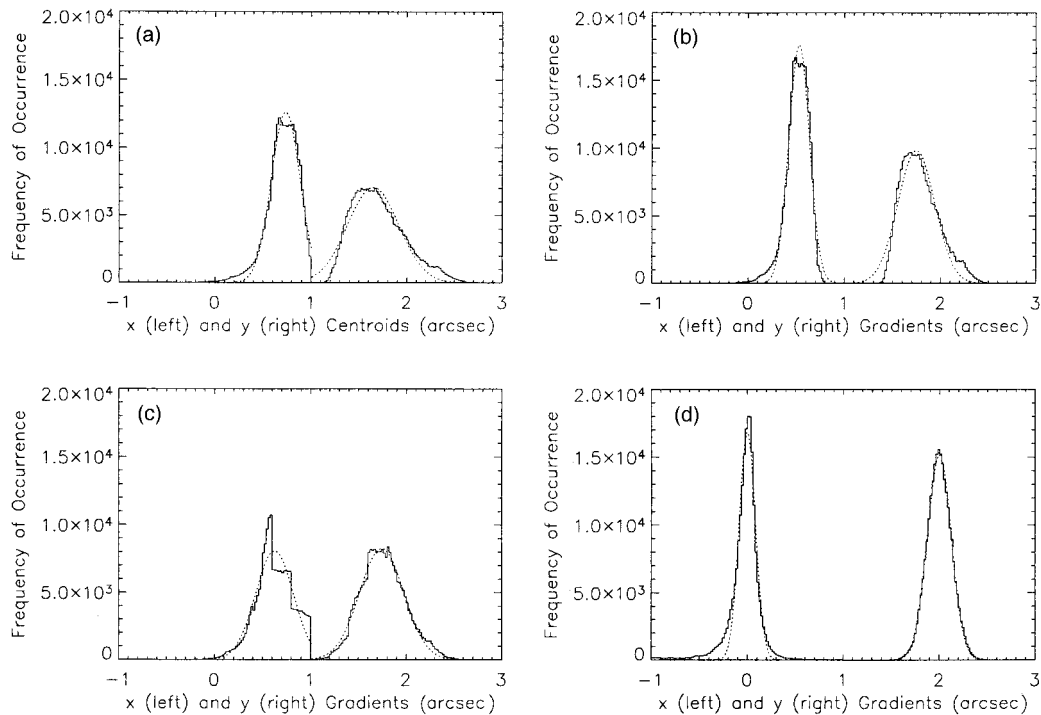


Fig. 4. Example of the frequency of occurrence of AA values for a set of 1000 frames of open-loop diagnostics data. In all cases, the solid curves are histograms of the observed quantities and the dotted curves are the best-fit Gaussians to these observations. The  $x$  components are shown on the left and the  $y$  components are shown on the right, offset by 2 units or 2 arcsec for clarity. (a) Measured centroids. Note that the static aberrations were not removed for this example. (b) AA reconstructed with the constant conversion factor method. (c) AA reconstructed with the inversion of Eq. (8). (d) Same as (c) but after removal of static aberrations.

The problem with this is that small changes of the centroid value cause large variations of the resulting AA values if the centroid values are large, as is the case for a large part of the open-loop data. This effect causes an amplification of noise and possibly large errors in the AA calculation. The result of the inversion is shown in Fig. 4(c). We can see that the two histograms have become much more symmetric and similar to each other. The large deviations from the Gaussian shape are not caused by noise but by static aberrations, as can be seen in Fig. 4(d) where the histograms are plotted after the removal of static aberrations. The curves now look much more Gaussian, although asymmetries still exist. We can also see that the difference in width of the  $x$  and  $y$  components remains. (This could, of course, be caused partially by the fact that the data set used for this example is only 1.5 s long—the usual problem with diagnostics data—and that  $x$  and  $y$  centroids represent atmospheric turbulence with different statistics.) Therefore use of open-loop data should be avoided.

On the contrary, TT-loop-closed data display a much more favorable behavior. We plotted  $x$  (on the left of each plot) and  $y$  (on the right of each plot, offset by 2 arcsec) components of the AA for a data set of 900 frames of telemetry data in Fig. 5. Figure 5(a) shows the AA calculated with the linear conversion approximation, and Fig. 5(b) shows the AA calculated through the inversion of Eq. (8). We can see that the

histograms are much more symmetrical and comparable between  $x$  and  $y$  components, even for the approximate AA reconstruction. The slight shifts of the curves with respect to the origin (as for Fig. 4, static aberrations were not removed in this example) are caused by noncommon path aberrations and corroborate the need for the conditioning even for TT-loop-closed telemetry data.

Differences between the curves in Figs. 5(a) and 5(b) appear small, and one might assume that use of a constant factor  $C_{\text{cent} \rightarrow \text{AA}}$  would be sufficient for the AA reconstruction. However, the  $r_0$  calculated from this particular data set is 18.8 cm if the linear conversion approximation is used, whereas  $r_0 = 14.9$  cm is found for the curve inversion method. Even for  $r_0$  values in the 15–20-cm range, the linear conversion approximation thus overestimates  $r_0$  by as much as 25% for the Keck AO systems. This error increases if  $r_0$  is smaller than for this particular example. In our analysis, we always perform the inversion of Eq. (8) for the AA reconstruction from the measured centroids.

A final detail that needs to be taken into account is the effect of noncommon path aberrations. The DM reference shape is usually not flat, but chosen so that it minimizes the effect of noncommon path aberrations on the science camera. Precalibrated centroid offsets are added to the measured centroid positions to account for these aberrations. As a result, the reference point of a given subaperture is not equal to

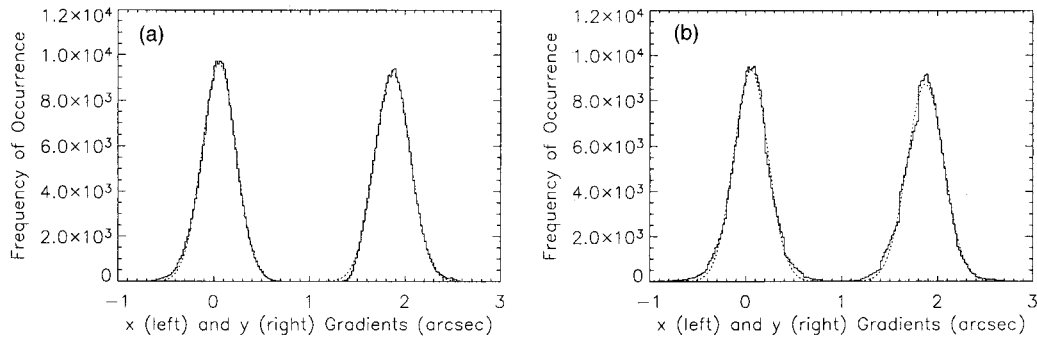


Fig. 5. Histograms of the AA values for a set of 900 frames of TT-loop-closed telemetry data. The data are represented in the same way as in Fig. 4. Static aberrations were not removed. (a) AA calculated with the linear conversion approximation, (b) AA calculated through the inversion of Eq. (8).

the zero point of the curve of Fig. 3. The effect on the measured  $r_0$  is usually small and can be neglected if one chooses to work with the linear conversion approximation. In combination with the inversion of Eq. (8), however, it occasionally causes instabilities of the Zernike coefficient reconstruction (see Section 5). The centroid offsets therefore have to be taken into account when this method is used.

#### D. Spot-Size Enlargement Due to Turbulence

Even after the AA reconstruction described in Subsection 3.C is done, one is not finished with the AA calibration. The centroid-to-AA conversion is highly dependent on the spot size, as we show in Fig. 3. The dotted curve is the theoretical curve for a spot size 0.25 arcsec larger than the best-fit value (that is, 1.51 arcsec), whereas the dashed curve is for a spot size 0.25 arcsec smaller than the best-fit value (2.01 arcsec). We can see that relatively small changes of the spot size produce large differences in the calibration curves. In fact, this strong dependence of the calibration on the spot size can produce one of the largest errors in the determination of atmospheric parameters from AO data if the spot size is not accurately known or if it changes. If, for example, the spot size is 1.36 arcsec and the value used in the calculation is 1.26 arcsec, the calculated  $r_0$  is approximately 10% larger than the real value for the Keck AO systems. Therefore it is extremely important that the spot-size calibration is known as accurately as possible, at least for AO systems equipped with a quadrant detector.

Because of this sensitivity of the calibration on the spot size, we need to take the seeing dependence of the spot into account. The value of 1.26 arcsec for  $\text{FWHM}_{\text{calib}}$  obtained in our calibration is associated with a point source. Atmospheric turbulence produces a spot FWHM of<sup>16</sup>

$$\text{FWHM}_{\text{turb}} = 0.98 \frac{\lambda_{\text{WFS}}}{r_0(\lambda_{\text{WFS}})}, \quad (10)$$

where  $\lambda_{\text{WFS}}$  is the wavelength of the light measured by the WFS and  $r_0(\lambda_{\text{WFS}}) = r_0(\lambda_{\text{WFS}}/0.5 \mu\text{m})^{6/5}$  is the atmospheric coherence length at this wavelength.

(Unless otherwise indicated, we always refer to turbulence parameters by their value at 0.5  $\mu\text{m}$  and denote them simply by  $r_0$ ,  $\tau_0$ , and so on.) Equation (10), of course, is an approximation as it applies to long-exposure images, which is certainly not correct for the WFS measurements. We use it nevertheless in the following paragraphs to illustrate the method and because no such analytical solution exists for the individual short exposures taken by the WFS.

At Keck,  $\lambda_{\text{WFS}} \approx 0.63 \mu\text{m}$ . The combination of  $\text{FWHM}_{\text{calib}}$  and  $\text{FWHM}_{\text{turb}}$  then yields an overall spot FWHM of 1.35 arcsec for  $r_0 = 20 \text{ cm}$  and 1.59 arcsec for  $r_0 = 10 \text{ cm}$ . If this spot enlargement is not taken into account, the errors in the  $r_0$  determination are 9% and 34%, respectively. The problem for the practical application, of course, is that  $r_0$  is initially not known and that a wrong spot size is therefore necessarily used in virtually all cases. An analytical solution of this problem is not possible because of the complexity of the  $r_0$  determination (see Sections 4 and 5). However, we can determine the real  $r_0$  iteratively. We first assume  $r_0$  to have a certain value. In fact, we can use the spot size from the calibration data, which implies  $r_0 = \infty$ . We then calculate  $r_0$  using the centroid-to-AA relation based on this spot size. This  $r_0$  is used to calculate a new estimate of the spot size, which, in turn, produces a new estimate of  $r_0$ . The process is iterated until it converges to a final value of  $r_0$ . An example of the convergence process for a particular telemetry data set taken with the Keck II telescope is shown in Table 1 in the columns denoted exact  $r_0$  and corresponding spot size. Note that the spot sizes shown are the real spot sizes on the WFS measured at a wavelength of 0.63  $\mu\text{m}$ , whereas the  $r_0$ 's are the standard values at 0.5  $\mu\text{m}$ . Convergence to within better than one part in  $10^4$  is obtained within six iterations. The corrected  $r_0$  differs from the original by approximately 13%.

The disadvantage of this iterative approach is that it requires us to run the entire data analysis process several times. This is not desirable for a real-time application. A better approach is to determine iteratively only the change of the constant conversion factor  $C_{\text{cent} \rightarrow \text{AA}}$  caused by the adjusted spot size. If

**Table 1. Demonstration of the Iterative Method that Accounts for the WFS Spot-Size Dependence on Atmospheric Turbulence<sup>a</sup>**

| Iteration | Exact $r_0$<br>(cm) | Corresponding Spot<br>Size (arcsec) | Approximate $r_0$<br>(cm) |
|-----------|---------------------|-------------------------------------|---------------------------|
| Initial   | $\infty$            | 1.260                               | $\infty$                  |
| 1         | 17.72               | 1.373                               | 17.72                     |
| 2         | 15.97               | 1.398                               | 15.96                     |
| 3         | 15.63               | 1.404                               | 15.60                     |
| 4         | 15.55               | 1.405                               | 15.52                     |
| 5         | 15.53               | 1.406                               | 15.50                     |
| 6         | 15.52               | 1.406                               | 15.50                     |
| 7         | 15.52               | 1.406                               | 15.50                     |

<sup>a</sup>The second and third columns show the  $r_0$  and spot-size FWHM obtained by performing the full iterative method. The fourth column contains the  $r_0$  values obtained by adjusting only the linear conversion approximation factor  $C_{\text{cent} \rightarrow \text{AA}}$ . Note that the spot sizes shown are the real spot sizes on the WFS measured at a wavelength of  $0.63 \mu\text{m}$ , whereas the  $r_0$ 's are the standard values at  $0.5 \mu\text{m}$ .

one were operating entirely in the linear regime,  $r_0$  would be proportional to  $C_{\text{cent} \rightarrow \text{AA}}^{-6/5}$ , and this iteration would be exact. However, even in the slightly nonlinear regime in which we usually operate with the Keck AO systems, this method works with high precision, as shown in the last column of Table 1. Because the difference between the approximate and exact solution is negligible and virtually no computer resources are necessary for this approach, the approximate method is preferred here.

As we mentioned above, use of Eq. (10) is not entirely correct because the individual image taken by a WFS subaperture is not a long-exposure image. Therefore the spot FWHM is expected to be smaller than the one used above. Furthermore, because the subaperture size is approximately  $56 \text{ cm} \times 56 \text{ cm}$ , a few times larger than the expected values of  $r_0$ , the spot will also be irregular and possibly contain speckles and scintillation. The combination of these two effects is one of the larger potential error sources of our analysis. If the WFS image size were reduced by 50% with respect to a long-exposure image, which is the maximum possible reduction predicted by theory,<sup>17</sup> Eq. (10) would yield upper limits to this error of 2%, 4.5%, 8%, and 18% for  $r_0$  values of 30, 20, 15, and 10 cm, respectively. The errors that we are likely to encounter for most conditions on Mauna Kea are therefore smaller than some of the other errors and approximations of the methods used and are usually acceptable. In addition, measurements of the WFS spot size while observing natural guide stars as well as the comparison of the results with long-exposure images (see Section 7) are consistent with use of Eq. (10) without modifications.

#### 4. Differential Image Motion

The determination of atmospheric parameters from AO system data suffers from the contamination of the data with system effects. The most important effects in the TT-loop-closed case, tracking errors and vibrations, influence only the global tilt of the wave

front. Reliable results can be found as long as we use methods that are not affected by global tilts. In this section and Section 5, we describe two methods that produce reliable estimates of the atmospheric coherence length  $r_0$ , the Zernike coefficient variances of the wave front, and, to a lesser degree of accuracy, the optical outer scale of turbulence  $\mathcal{L}_0$ .

#### A. Theoretical Background

Use of DIM to calculate  $r_0$  was first put into practice by Sarazin and Roddier.<sup>16</sup> It is based on the measurement of the DIM between two small apertures with a vector separation  $\mathbf{x}$  that equals a few times the aperture diameters  $d$ . One can calculate  $r_0$  from the rms difference of the image motion between the two apertures. If the two apertures are part of a larger aperture, this method has the advantage that the results are independent of instrument vibrations or tracking errors. The quadrant detector WFSs of the Keck AO systems measure the AA, and therefore the image motion, of the incoming wave front at a large number of subapertures and at fast frame rates. The WFS measurements are ideally suited for a determination of  $r_0$ .

A detailed overview of the DIM method, as well as a description of the data analysis, is given by Tokovinin.<sup>18</sup> Here, we present only the parts of this method that are important for the practical implementation at an AO system. The basis of our determination of  $r_0$  is the spatial structure function of the DIM,  $D_{\text{AA}}(\mathbf{r})$ , where  $\mathbf{r} = \mathbf{x}/d$ .  $D_{\text{AA}}(\mathbf{r})$  can be derived from the covariance of the AA differences between two apertures that are separated by a distance  $\mathbf{r}$ . This covariance is given by<sup>19</sup>

$$B_{\text{AA}}(\mathbf{r}) = \lambda^2 \iint d\mathbf{f}(\mathbf{f} \cdot \mathbf{u})^2 W_{\phi}(\mathbf{f}) G(\mathbf{f}) \exp(2\pi i \mathbf{f} \cdot \mathbf{r}). \quad (11)$$

Here,  $\lambda$  is the wavelength,  $\mathbf{f}$  is the spatial-frequency vector,  $\mathbf{u}$  is a unit vector in the direction in which the AA is measured,  $W_{\phi}(\mathbf{f})$  is the phase power spectrum, and  $G(\mathbf{f})$  is the point-spread function of an individual aperture. For all examples presented in this paper we follow Ref. 19 in assuming that the phase power spectrum is given by the von Kármán spectrum

$$W_{\phi}(\mathbf{f}) = 0.0229 r_0^{-5/3} (f^2 + f_0^2)^{-11/6}, \quad (12)$$

where  $f = |\mathbf{f}|$  and  $f_0 = 1/\mathcal{L}_0$ . Note that use of the von Kármán spectrum is arbitrary to a certain degree as the exact shape of the turbulence phase power spectrum is not known for large separations.  $G(\mathbf{f})$  is given by

$$G_{\circ}(\mathbf{f}) = \left[ \frac{2J_1(\pi d f)}{\pi d f} \right]^2 \quad (13)$$

for a circular aperture of diameter  $d$  and by

$$G_{\square}(\mathbf{f}) = \left[ \frac{\sin(\pi d f_x)}{\pi d f_x} \right]^2 \left[ \frac{\sin(\pi d f_y)}{\pi d f_y} \right]^2 \quad (14)$$

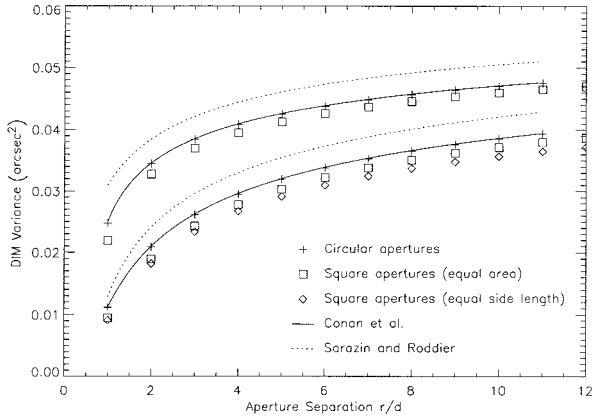


Fig. 6. Longitudinal (top set) and transverse (bottom set) DIM structure functions ( $G$  tilt) for a number of different cases. Dotted curves, approximate result from Sarazin and Roddier;<sup>16</sup> solid curves, analytical result of Conan *et al.*<sup>19</sup> for circular apertures; crosses, numerical simulation of the analytical results; squares, numerical simulation for square apertures with areas equal to those of the circular apertures; diamonds (only transverse DIM shown), numerical simulation for square apertures with a side length equal to the diameter of the circular aperture. All results are calculated with  $d = 56.25$  cm,  $\lambda = 0.5$   $\mu\text{m}$ ,  $r_0 = 0.2$  m, and an infinite outer scale.

for a square aperture of side length  $d$ . The final step, calculating the variance of the DIM  $\sigma_d^2$ , is done with

$$D_{AA}(\mathbf{r}) = 2[B_{AA}(0) - B_{AA}(\mathbf{r})]. \quad (15)$$

Combining Eqs. (11)–(15), one finds

$$D_{AA}(\mathbf{r}) = \lambda^2 r_0^{-5/3} d^{-1/3} \mathcal{F}(r, f_0), \quad (16)$$

where  $\mathcal{F}(r, f_0)$  is a function of the aperture separation and the outer scale of turbulence that can be evaluated analytically for special cases.<sup>18,19</sup> Examples of structure functions for different geometries and infinite outer scale ( $f_0 = 0$ ) are given in Fig. 6. For reference, the original results of Sarazin and Roddier,<sup>16</sup> which were calculated under the approximation of large separations, are shown as dotted curves.

Conan *et al.*<sup>19</sup> obtain their results by using the spherical symmetry of all components in Eq. (11) for the case of circular apertures and evaluating the integral analytically using Mellin transforms. Thus they obtain a general expression in the form of a power series of terms  $r/d$ ,  $rf_0$ ,  $df_0$ , and combinations thereof. When using the subapertures of a Shack–Hartmann sensor to calculate the DIM, we are dealing with square apertures instead of circular apertures. The reduction of Eq. (11) to a one-dimensional integral cannot be performed easily and, because only the values for a small number of separations in a fixed geometry are needed, the easiest solution is to evaluate Eq. (11) numerically. The crosses in Fig. 6 show the results of this numerical integration for infinite outer scale and circular apertures. (This case serves simply as a verification that the numerical integration is performed correctly.

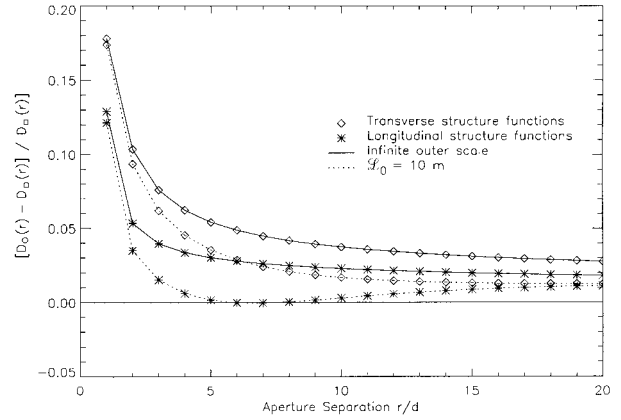


Fig. 7. Relative difference between the DIM structure functions of square and circular apertures of equal area. The results are calculated for square apertures of  $d = 56.25$ -cm side length,  $\lambda = 0.5$   $\mu\text{m}$ , and  $r_0 = 0.2$  m.

The crosses lie, as expected, on the solid curves.) The squares show  $D_{AA}(\mathbf{r})$  for square subapertures with areas equal to those of the circular apertures. The errors made by use of the analytical results from Conan *et al.*<sup>19</sup> for square subapertures are shown for two values of  $\mathcal{L}_0$  in Fig. 7. We can see that the errors are generally small, but that they can be almost 20% for  $r/d = 1$ . In the calculation of  $r_0$  from DIM using square apertures, one needs to decide if this difference is acceptable—in which case one can use analytical results. In our analysis we work with the exact results of the numerical integrations for square subapertures and do not approximate the squares as circles. (Note that the values shown as squares in Fig. 6 are calculated for square apertures with the same area as the circular apertures shown as crosses.) By contrast, the case of square apertures with side lengths equal to the diameters of circular apertures are shown as diamonds (transverse structure function only).

To conclude this subsection, we point out that it might be necessary to use the  $Z$  tilt instead of the  $AA$  (or  $G$  tilt) for systems that do not use a quadrant detector for the determination of the tilt. The difference in DIM structure functions for  $G$  and  $Z$  tilt can be as high as 15%.<sup>18</sup> At Keck, where a simple quadrant cell algorithm is used, the quantity measured by the WFS is usually considered to be close to the  $G$  tilt.<sup>20</sup> Even this, however, is only an approximation if speckles and scintillation occur on the WFS. The deviation of the measured quantity from the  $G$  tilt is therefore one of the larger error sources of the DIM method.

## B. Data Analysis

The main advantage of using an AO system instead of a standard differential image motion monitor is that, instead of measuring the  $AA$  for only one pair of apertures, we have measurements of the  $AA$  at a few hundred subapertures available for any WFS frame. We can calculate many points of the structure func-

tion and perform a least-squares fit to the theoretical shape of the curve. The overall scaling factor then yields  $r_0$ , and the shape of the curve can theoretically be used to calculate  $\mathcal{L}_0$ . The shape of the curve, however, is only weakly dependent on the outer scale.<sup>21</sup> The calculated value of  $\mathcal{L}_0$  therefore has to be considered as only a rough estimate.

The structure function of the data,

$$D_{AA}(\Delta\mathbf{r}) = \langle [\alpha(\mathbf{r}) - \alpha(\mathbf{r} + \Delta\mathbf{r})]^2 \rangle, \quad (17)$$

where  $\alpha(\mathbf{r})$  denotes the AA at position  $\mathbf{r}$  and  $\langle \rangle$  is the ensemble average, can be calculated in two ways. One can use the brute force method of calculating the difference in AA for all pairs separated by  $\Delta\mathbf{r}$  and taking the average of these values. The second method is to calculate the covariance of the data with fast-Fourier transforms (FFTs) and the Wiener-Khinchin theorem. The fast-Fourier transform also has to be divided by the aperture transfer function (the autocorrelation of the aperture function) to account for sampling effects. The structure function is then obtained by use of Eq. (15). We use the fast-Fourier transform method for our analysis because it is faster than even calculating only the longitudinal and transverse structure functions with the brute force method and, at the same time, it yields the structure function for all directions of  $\Delta\mathbf{r}$ . This analysis is performed separately for  $x$  and  $y$  components of the AA.

We then perform a least-squares fit of the data to the theoretical results. As the goal of this application is to produce a tool that, in the end, will run almost in real time while the AO system is operating, saving computer resources (both memory and CPU time) is a major concern. We calculated templates of the theoretical structure function for the given geometry of the AO systems for different values of  $\mathcal{L}_0$  and performed fits to these templates, taking into account contributions from WFS noise.<sup>18</sup> For a standard differential image motion monitor with only two apertures, this noise needs to be estimated and subtracted from the structure function. When using an AO WFS with a large number of subapertures, however, we can include the noise as an additional parameter in the least-squares fit as long as the noise of different subapertures is uncorrelated.

For our data, the major contributions to the noise are readout noise and photon noise. Other noise sources are dark current, flat-fielding errors (flat fielding is usually not performed for AO WFSs), and segment vibrations. Dark current can be ignored for bright stars. Although flat-fielding noise stems from the nonuniform pixel sensitivities of the WFS that are often correlated, it can usually be neglected for modern CCDs. Segment vibrations will introduce partially correlated noise, in particular for small separations  $\Delta\mathbf{r}$  (for example, for subapertures that happen to lie on the same segment and because the vibrations of nearby segments are likely to be at least partially correlated). The analysis of vibrations at Keck is in progress and no certain results exist.

However, preliminary results of all vibrations, global and segment, indicate that the error made by neglecting vibrations is small compared with other approximations made in our analysis. This will then be true to a much higher degree of accuracy if only the correlated part of segment vibrations is of concern. If we finally assume that the rms single-subaperture noise  $\sigma_N$  is the same for all subapertures, the DIM structure function becomes

$$D_{AA}(\Delta\mathbf{r}) = \begin{cases} \langle [\alpha(\mathbf{r}) - \alpha(\mathbf{r} + \Delta\mathbf{r})]^2 \rangle + 2\sigma_N^2 & \Delta\mathbf{r} \neq 0 \\ 0 & \Delta\mathbf{r} = 0 \end{cases} \quad (18)$$

For each structure function template we can thus perform a least-squares fit of the data by minimizing

$$\sum_i \frac{[(Ct_i + a) - d_i]^2}{\sigma_i^2}. \quad (19)$$

Here  $d_i$  denotes a point of the observed structure function,  $t_i$  is the corresponding value of the theoretical structure function, and the summation is over all data points. The constant  $C$  is an overall scaling factor that is used to calculate  $r_0$  ( $r_0 \propto C^{-3/5}$ ; all templates are calculated with  $r_0 = 1$  m) and  $a$  is equal to  $2\sigma_N^2$ . The rms error associated with data point  $d_i$  is denoted  $\sigma_i$  in expression (19). We do not know this error until the fit is performed, after which it can be found from the constant  $a$ . However, only the relative values of these errors matter for the fit. These can be found from the fact that  $\sigma_i^2 \propto 1/N_i$ , where  $N_i$  is the number of data points used to calculate  $d_i$ . We calculate  $N_i$  through the aperture transfer function. Finally, the central value of the structure function  $D_{AA}(0)$  needs to be treated separately, as the noise term  $a$  does not apply to this data point. In practice, we simply omit it from the fit by assigning it an error  $\sigma_i = \infty$ . This omission does not decrease the accuracy of the fit because the central point is by definition always zero and therefore contains no information.

The fit needed to minimize expression (19) is identical to a chi-squared fit of a straight line, and the two fitted quantities are given by

$$C = \frac{SS_{td} - S_t S_d}{SS_{tt} - S_t^2}, \quad a = \frac{S_d - CS_t}{S}, \quad (20)$$

with

$$\begin{aligned} S &= \sum_i \frac{1}{\sigma_i^2}, & S_t &= \sum_i \frac{t_i}{\sigma_i^2}, & S_d &= \sum_i \frac{d_i}{\sigma_i^2}, \\ S_{td} &= \sum_i \frac{t_i d_i}{\sigma_i^2}, & S_{tt} &= \sum_i \frac{t_i^2}{\sigma_i^2}. \end{aligned} \quad (21)$$

The fit is performed for all different values of  $\mathcal{L}_0$  for which templates exist. The rms difference between data and best-fit theoretical results is then calculated for all templates, and a simple linear interpolation between templates is performed. The parameters corresponding to these curves yield our estimates of

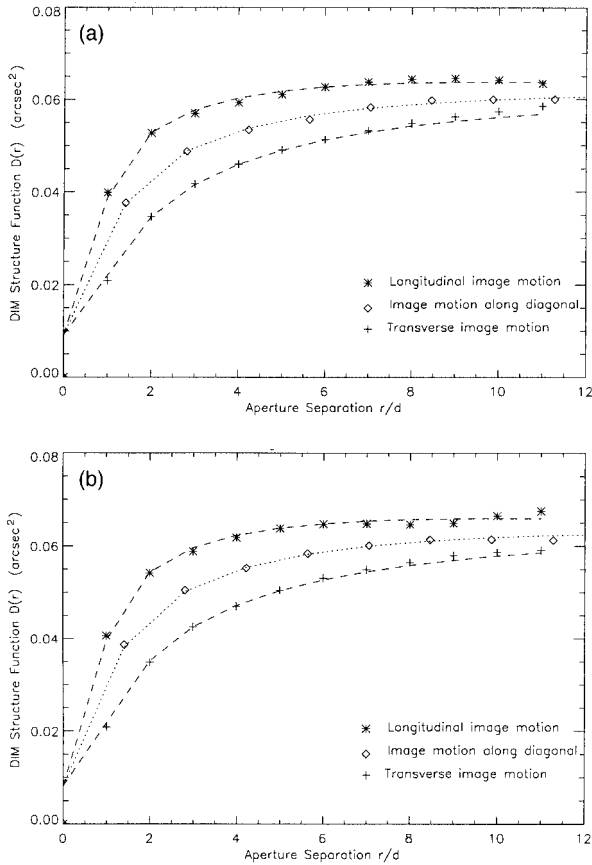


Fig. 8. Example of DIM structure functions calculated from a set of 600 frames of telemetry data. Symbols represent the data and the curves represent the best-fit theoretical curves. (a)  $x$  centroids, (b)  $y$  centroids. The fits were performed simultaneously for the entire two-dimensional structure function. The fit parameters are  $r_0 = 16.5$  cm,  $\mathcal{L}_0 = 39$  m, and  $\sigma_N = 0.067$  arcsec for the  $x$  centroids and  $r_0 = 15.9$  cm,  $\mathcal{L}_0 = 37$  m, and  $\sigma_N = 0.064$  arcsec for the  $y$  centroids.

$r_0$ ,  $\mathcal{L}_0$ , and  $\sigma_N$ . An example of such a fit to experimental data is shown in Fig. 8, demonstrating excellent agreement between data and theory.

### 5. Zernike Decomposition

Another method for the analysis of atmospheric turbulence with AO telemetry data is the decomposition of the wave-front phase into Zernike modes. The Zernike decomposition (ZD) method, like the DIM method, is insensitive to telescope vibrations and tracking errors, which both affect only the tip and the tilt Zernike modes. In addition, segment vibrations that are uncorrelated for different segments cancel out on average and have no effect on the results. Higher-order vibrations of the overall structure as well as correlated segment vibrations, in principle, can corrupt the results. A qualitative analysis of the power spectra of these modes, however, does not show any discernible vibration spikes in our data. The ZD method therefore is a reliable technique for the characterization of atmospheric turbulence.

The basis of the ZD method is the calculation of the

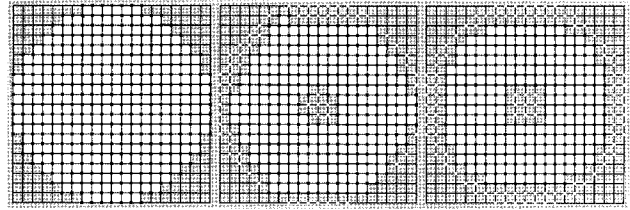


Fig. 9. Subaperture configurations of the Keck AO systems. The grids represent the  $20 \times 20$  subapertures of the WFSs. The black and white dots indicate the positions of the 349 actuators of the DM, located at the corners of the subapertures. Marked as white squares are, on the left, all 308 subapertures that are surrounded by four actuators; in the center are the 241 fully illuminated apertures for a particular orientation of the Keck pupil; on the right is a subset of 208 subapertures that are always fully illuminated. The configuration on the right, forming an approximately 9-m subpupil, is used for the reconstruction of the phase in our analysis.

variances of individual Zernike modes. One obtains  $r_0$  by comparing these variances with theoretical values.<sup>22,23</sup> The problems lie, as before, in the practical issues of calculating the Zernike coefficients  $C_{Z,i}$  while excluding instrument effects. The first step in the ZD is the reconstruction of the wave-front phase  $\phi(\mathbf{r})$  from the measured wave-front AA. This can be done either by using the AA and an appropriate reconstruction matrix or by using the wave-front phase telemetry output of the AO system directly. (If telemetry data are used, one has to make sure that only the reconstructed wave front is recorded and not the actuator commands, as the latter usually contain the effects of temporal filter functions that account for the system bandwidth. The actuator commands, at least for TT-loop-closed data, contain nonatmospheric contributions and should not be used directly with the ZD method.) In our analysis, we prefer the first approach for two reasons. First, it delivers as a by-product the eigenmodes of the reconstruction matrix, which, as we show below, is required for the ZD. Second, recording the phase data in addition to the AA (which we need for the DIM method) increases the size of the already large amount of data by almost a factor of 2. The increase in calculation time needed for the phase reconstruction matrix multiplication, in our case, is preferable to the additional disk space required for storing both AA and phases.

Our phase reconstruction is a basic geometric reconstruction.<sup>24</sup> The Keck AO systems use the Fried geometry; that is, the actuators are at the corners of the subapertures. In Fig. 9, the  $20 \times 20$  subapertures of the WFS are shown three times. The 349 actuators of the DM are marked as black or white dots. The left plot highlights all 308 subapertures that are surrounded by four actuators. Because of the hexagonal shape of the Keck primary mirrors, only 241 of those subapertures are fully illuminated at any time (see center plot). As the pupil rotates on the WFS, different sets of subapertures are illuminated at different times. The matrices required for the ZD would have to be recalculated for each of these

configurations. For the sake of minimizing computation time, we therefore restrict ourselves to the set of 208 subapertures and 248 actuators shown on the right of Fig. 9, which are always entirely illuminated and form an approximately 9-m-diameter subpupil of the Keck aperture. This is a compromise between signal-to-noise ratio and computational efficiency. Because data sets usually contain hundreds of thousands of individual AA measurements, it does not significantly reduce the signal-to-noise ratio of the data.

We now define the matrix  $\mathbf{A}$  that relates the number of AA measurements  $N_{\text{AA}}$  to the number of phase points at the actuator positions  $N_{\phi}$ . For a given subaperture  $j$ , the phase (in radians at wavelength  $\lambda$ ) is given by

$$\alpha_j = \frac{\lambda}{4\pi d} (\phi_{\text{ur}} + \phi_{\text{lr}} - \phi_{\text{ul}} - \phi_{\text{ll}}), \quad (22)$$

$$\beta_j = \frac{\lambda}{4\pi d} (\phi_{\text{ur}} + \phi_{\text{ul}} - \phi_{\text{lr}} - \phi_{\text{ll}}), \quad (23)$$

where  $\alpha_j$  and  $\beta_j$  are the  $x$  and  $y$  components of the AA, respectively, and  $d$  is the linear aperture size. The  $\phi$  are the phases in the corners of the subaperture, where the subscripts stand for upper right (ur), upper left (ul), lower right (lr), and lower left (ll). Combining Eqs. (22) and (23) for all subapertures, we can write them as  $\mathbf{g} = \mathbf{A}\Phi$ , where  $\mathbf{g}$  is a vector containing all  $x$  and  $y$  components of the AA and  $\Phi$  is a vector containing all phases. The matrix  $\mathbf{A}$  is defined by Eqs. (22) and (23) and has the dimension  $2N_{\text{AA}} \times N_{\phi}$ . (For reference, for the aperture shape shown on the right side of Fig. 9,  $\mathbf{A}$  is a  $416 \times 248$  matrix.) The phase reconstruction matrix, that is, the matrix used to calculate the phases from the AA measurements, is simply  $\mathbf{A}^{-1}$ , the (pseudo)inverse of  $\mathbf{A}$ , which can be found by singular value decomposition.<sup>25</sup>

The direct calculation of coefficients  $C_{Z,i}$  of the Zernike modes  $Z_j(\mathbf{r})$  with<sup>22</sup>

$$C_{Z,i} = \int d\mathbf{r} W(\mathbf{r}) \phi(\mathbf{r}) Z_j(\mathbf{r}), \quad (24)$$

where  $W(\mathbf{r}) = 1/\pi$  inside the aperture and zero outside the aperture, is not possible because the aperture used is not circular. The Zernike modes therefore do not form an orthogonal basis of the aperture, and Eq. (24) does not yield  $C_{Z,i}$  but rather a linear combination of Zernike coefficients. Even for the aperture shown on the right side of Fig. 9, this effect creates errors that preclude an accurate determination of  $r_0$ . We therefore use the eigenmodes  $M_i(\mathbf{r})$  of the phase reconstruction matrix, which we obtain also from the singular value decomposition, as our basis set.

If we were interested only in  $r_0$ , it would be most straightforward to calculate the expected variances of these eigenmodes based on the chosen turbulence model and thus obtain  $r_0$  by comparison with the measured variances. However, we are also inter-

ested in other properties of turbulence, such as the power spectra of Zernike modes, for which a reconstruction of the Zernike coefficients  $C_{Z,i}$  is necessary. We therefore reconstruct the Zernike coefficients from the coefficients  $C_{M,j}$  of modes  $M_i(\mathbf{r})$ . This reconstruction is based on the assumption that the Zernike modes, although not orthogonal on the aperture used, are nevertheless linearly independent. This assumption is certainly true for all but the highest-order modes, for which the variances of atmospheric turbulence are so small that their effect can be neglected. Each mode  $M_j(\mathbf{r})$  then always produces the same linear combination of Zernike modes and

$$C_{M,j} = \sum_{i=0}^{N-1} b_{ij} C_{Z,i}, \quad (25)$$

with

$$b_{ij} = \frac{\int Z_j(\mathbf{r}) M_i(\mathbf{r}) d\mathbf{r}}{\int M_i(\mathbf{r}) M_i(\mathbf{r}) d\mathbf{r}}, \quad (26)$$

which is a unique relationship between  $C_{M,j}$  and  $C_{Z,i}$ , independent of the values of the coefficients. Thus we can find the Zernike coefficients from the  $C_{M,j}$  by inverting the matrix  $\mathbf{B}$  containing all  $b_{ij}$ . This inversion is again performed by singular value decomposition.

The matrices used to find the phase, to calculate the  $C_{M,j}$ , and to reconstruct the  $C_{Z,i}$  can now be combined into a single reconstruction matrix  $\mathbf{R}$  with

$$\mathbf{c}_Z = \mathbf{R}\mathbf{g} = \mathbf{BMA}^{-1}\mathbf{g}, \quad (27)$$

where  $\mathbf{c}_Z$  is a vector containing all Zernike coefficients and  $\mathbf{M}$  is a matrix calculating the  $C_{M,j}$  from the wave-front phase. Thus only one matrix multiplication is necessary to find the Zernike coefficients directly from the AA. The dimensions of  $\mathbf{R}$  are  $N_{\text{AA}} \times N_Z$ , where  $N_Z$  is the number of Zernike modes to be reconstructed and needs to be chosen carefully. The effect of using different  $N_Z$  is demonstrated in Fig. 10 where we plotted the variances calculated from a sample telemetry data set taken with the Keck II telescope. The asterisks (data) of the left plot show the Zernike variances if the first 6 radial orders (21 Zernike modes) are used to calculate  $C_{Z,j}$ . The first three modes (piston, tip, and tilt) are excluded from the plot. For comparison, the solid line indicates the theoretical values for Kolmogorov turbulence and the best-fit  $r_0$ . We can see that the observed variances follow the expected plateaulike behavior,<sup>22</sup> but that the observed values for radial orders 5 and 6 are significantly below the expected values due to correlations with higher-order modes. The right plot shows the observed and theoretical variances, offset by 15 modes to the right for clarity, when 55 modes (10 radial orders) are used in the calculation. The data follow the theoretical behavior for 8 radial or-

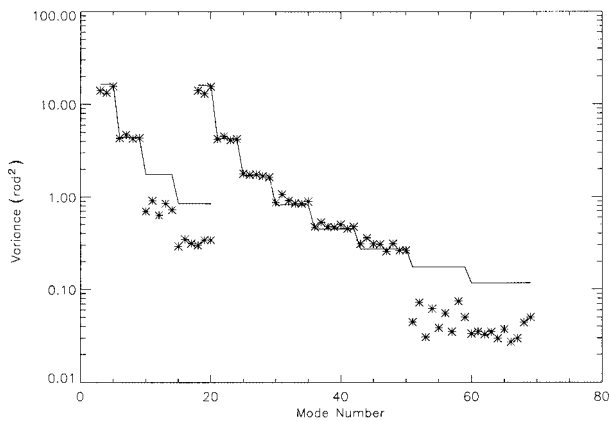


Fig. 10. Examples of the calculation of variances of Zernike modes from the eigenmodes of the phase reconstruction matrix by use of different numbers of Zernike modes. Left, with 6 radial orders (21 modes); right, with 10 radial orders (55 modes), offset by 15 modes to the right for clarity. The asterisks are results from telemetry data and the solid curves indicate theoretical values for Kolmogorov turbulence. The two highest radial orders of each plot are corrupted by correlations with modes not included in the calculation. This is true independent of the number of modes used.

ders whereas the last two radial orders again differ from theory. (The fact that observed values are smaller than the theoretical values for exactly the last two radial orders is due to the specific shape of the aperture used.) If even more modes are used, computational errors begin to increase significantly. For the Keck data and aperture shapes, using 10 radial orders ( $N_Z = 55$ ) in the reconstruction and calculating  $r_0$  for radial orders 3–8 (33 modes) appears to be a good compromise between obtaining the variances of as many modes as possible and computational errors.

To conclude this section, we point out two more features of Fig. 10. First, variations of the observed variances within a given radial order are reproducible between the different curves. However, they are not the same as those represented in Fig. 10 if one looks at different data sets. Thus they are caused by real atmospheric variations and not by systematic errors or computational artifacts. Second, if we compare the 10-radial-order curve to the variances expected for Kolmogorov turbulence (solid line), we can see that the low-order modes are on average slightly below the theoretical curve whereas the high-order modes are above the curve. This is caused by a finite outer scale of turbulence  $\mathcal{L}_0$ . In our analysis, we therefore calculate  $r_0$  values from the Zernike variances using both the Kolmogorov and the von Kármán turbulence spectra.<sup>22,23</sup> The Kolmogorov results are used to characterize the reduction of the power in the low-order modes due to the finite outer scale, whereas the most reliable value for  $r_0$  is found using the van Kármán spectrum, which also yields an estimate of  $\mathcal{L}_0$ . Values for both  $r_0$  and  $\mathcal{L}_0$  found using this method are in excellent agreement with

those from the DIM method, as we demonstrate in Section 7.

## 6. Temporal Analysis

### A. Atmospheric Coherence Time $\tau_0$

The atmospheric coherence time  $\tau_0$  is defined as the time interval over which the wave-front phase changes by 1-rad rms. As such, it cannot directly be calculated from the wave-front AA but must be obtained from the temporal variance of the reconstructed phase. The full (that is, tilt included) phase, in principle, is necessary for this, but this is corrupted by all effects that introduce time-varying global tilts, in particular by telescope vibrations (as before, we can ignore segment vibrations). This problem can be dealt with by removing any residual global tilt artificially from the reconstructed phase. The tilt-removed phase, of course, is missing a part of the signal of the real atmospheric phase variations and  $\tau_0$  will in general be overestimated. However, the global tilt over a 10-m aperture changes little over time scales comparable to  $\tau_0$ , which is typically a few milliseconds at  $\lambda = 0.5 \mu\text{m}$ . The error made by using the tilt-removed wave front is small. Results should nevertheless be taken with caution at this point. More reliable estimates of  $\tau_0$  should be obtainable from the analysis of temporal power spectra. The first qualitative results of such power spectra have already been presented.<sup>21</sup> A quantitative analysis of the spectra is beyond the scope of this paper and will be addressed in future research.

The calculation of  $\tau_0$  is performed by calculating the temporal phase structure function  $D_\phi(\Delta t)$  for a few values of  $\Delta t$  and determining by interpolation the point at which it equals  $1 \text{ rad}^2$ . As mentioned above, this analysis as well as all other temporal analyses can be done only for high-frame-rate diagnostics data and not for low-frame-rate telemetry data.

### B. Finite Exposure Time

At full frame rate, the exposure time of the Keck WFS data is approximately 1.5 ms. This is, in general, sufficiently short that no correction for the averaging effect due to the finite exposure time<sup>18</sup> needs to be applied. However, there do exist conditions under which the seeing varies so quickly that even a 1.5-ms exposure cannot be considered instantaneous. Furthermore, a correction needs to be applied if the AO system uses faint guide stars, for which it operates at lower frame rates. The minimum frame rate of the Keck AO systems is 55 Hz.

The exposure time correction is done by averaging consecutive frames of diagnostics data in sets of two and thus creating a data set of half of the original frame rate. One then calculates the quantity of interest—this can be either the DIM structure function or the Zernike mode variances—for both the original data set  $q_1$  and for the binned data  $q_2$ . The corrected quantity is then given by  $q = q_1^2/q_2$  or, as it has also been found that this correction overshoots the real value of  $q$ , by  $q = q_1^{1.75}q_2^{-0.75}$ .<sup>18</sup> For all

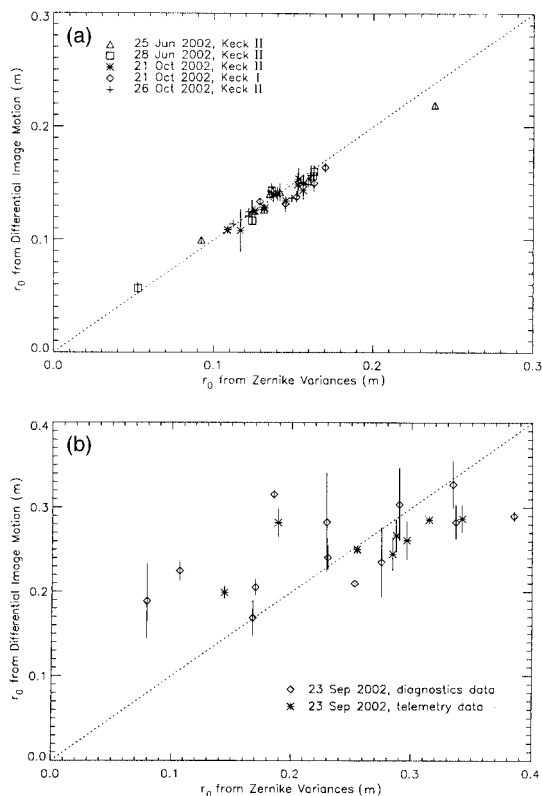


Fig. 11. Comparison of values of  $r_0$  found using the DIM method (ordinate) and the ZD method (abscissa). The full lengths of the vertical bars indicate the differences between the  $r_0$  values determined from  $x$  and  $y$  centroids by the DIM method. (a) Results obtained from telemetry data during the nights of 25 June, 28 June, 21 October, and 26 October 2002 with the Keck II AO system and on 21 October 2002 with the Keck I AO system. The data sets are between 56 and 294 s in length and are taken at frame rates between 4 and 6 Hz. (b) Results obtained with the Keck II AO system on 23 September 2002 with diagnostics data and telemetry data taken at frame rates between 2 and 2.5 Hz.

conditions that we have encountered so far, both corrections are negligible because of the large size of the Keck subapertures. If a large correction is ever found to be necessary, we can determine the best correction method by binning larger numbers of data frames, calculating  $q_n$  for all these cases, and extrapolating  $q$ .

## 7. Results

### A. Internal Consistency Checks with Telemetry Data

We begin the description of sample results with consistency checks of the DIM and ZD methods, which can be considered independent for this purpose. A comparison of results found with the two methods is shown in Fig. 11. In Fig. 11(a) we plot values of  $r_0$  obtained from telemetry data during five different nights. We can see that there exists excellent agreement between the values found using the two methods. Although this constitutes, of course, no evidence that these values correspond to the real  $r_0$ , it does show that the methods were implemented

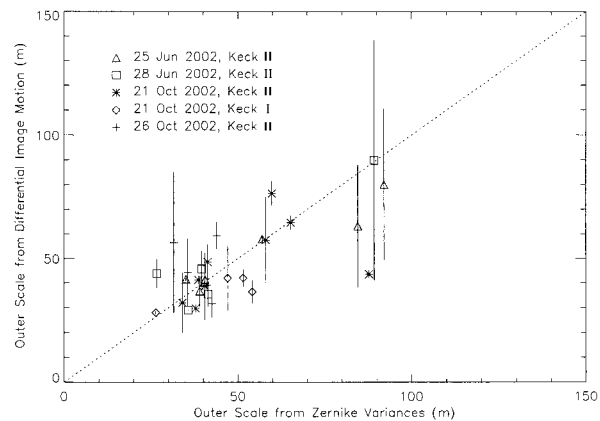


Fig. 12. Comparison of values of  $\mathcal{L}_0$  found with the DIM method (ordinate) and the ZD method (abscissa). The full lengths of the vertical bars indicate the differences between the  $\mathcal{L}_0$  values determined from  $x$  and  $y$  centroids with the DIM method. Results were obtained from telemetry data during the nights of 25 June, 28 June, 21 October, and 26 October 2002 with the Keck II AO system and on 21 October 2002 with the Keck I AO system. A total of six data points with  $\mathcal{L}_0$  values greater than 150 m were omitted from the plot to decrease the plot range.

correctly and consistently. The remaining potential error sources are global effects such as the conditioning or the overall calibration of the data. This is assessed in Subsection 7.B.

The differences between the  $r_0$  values found from the  $x$  and  $y$  centroids with the DIM method are indicated by the vertical bars in Fig. 11. As  $x$  and  $y$  centroids are independent data sets, the generally short lengths of the bars show that the data sets are statistically representative for the given turbulence conditions. We found that, for this to be true, telemetry data need to be taken at frame rates of at least 4 Hz and that at least several tens of seconds of data are necessary. For comparison, results obtained from telemetry data taken at frame rates between 2 and 2.5 Hz (asterisks) and of diagnostics data sets of 1.5 s length (diamonds) are shown in Fig. 11(b). These data do not sample turbulence with sufficiently high frequency or for sufficiently long amounts of time to produce consistent results.

A comparison of values of the outer scale  $\mathcal{L}_0$  obtained from telemetry data is shown in Fig. 12. The consistency of the results is again good given that the turbulence spectrum depends only weakly on the outer scale, in particular for large values of  $\mathcal{L}_0$ . We have thus shown that our methods of analyzing telemetry data are consistent with each other and appear to be implemented correctly. We next present the comparison with results from long-exposure images.

### B. External Consistency Checks with Telemetry Data

During the night of 26 October 2002, we took simultaneous telemetry data and long-exposure images with the Near-Infrared Camera 2 (NIRC2) camera using the Keck II telescope. The images were taken in the H band at a wavelength of 1.63  $\mu\text{m}$ . The

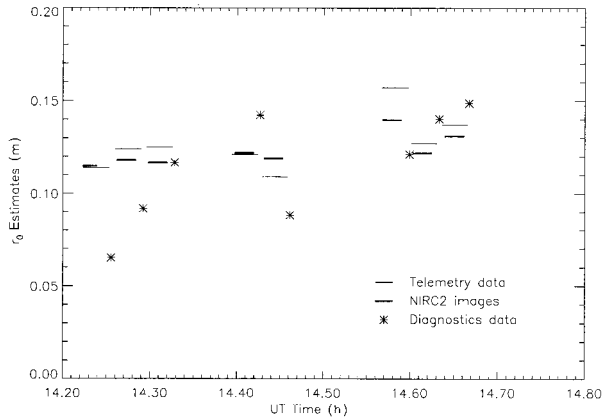


Fig. 13. Values of  $r_0$  obtained on 26 October 2002. The thin bars are results from telemetry data with the lengths of the bars indicating the lengths of the data sets. Thick bars are results from NIRC2 long-exposure images. The asterisks show  $r_0$  values calculated from 1.5-s diagnostics data sets.

results are shown in Fig. 13. Thin horizontal bars are the results for  $r_0$  obtained from telemetry data, where the lengths of the bars indicate the durations of the data sets. Thick bars show  $r_0$  values from NIRC2 images that we obtained by fitting the theoretical TT removed point-spread function to the images. Asterisks are the results from 1.5-s diagnostics data sets (discussed in Subsection 7.C).

We can see that there is excellent agreement between the telemetry and the NIRC2 results. The average difference between  $r_0$  values is 5%. The fact that NIRC2 images usually produce slightly smaller values for  $r_0$  than telemetry data is expected, as static optical aberrations are removed from the telemetry data but cannot be removed from the images. On the other hand, most of the differences can be accounted for by changes in the spot size as small as 0.02 arcsec, which is smaller than the accuracy of the spot-size calibration. Overall, the differences between the results are well within the error limits predicted in Section 3. Similar comparisons performed in earlier nights produce the same kind of results, with the average errors generally similar to those shown in Fig. 13 and the largest errors in the 10–15% range. Simultaneous open-loop data taken with the Keck I and Keck II AO systems also show good agreement with each other and with first results from a closed-loop telemetry data analysis. We thus arrive at the conclusion that our methods produce reliable absolute estimates of  $r_0$ .

### C. Diagnostics Data

We have mentioned that diagnostics data do not provide statistically representative samples of the turbulence conditions. This was demonstrated in Fig. 11 and can also be seen in Fig. 13, where the results of diagnostics data sets taken directly after each telemetry data set are shown as asterisks. To arrive at these results, the time averages of close-to-simultaneous telemetry data sets were subtracted

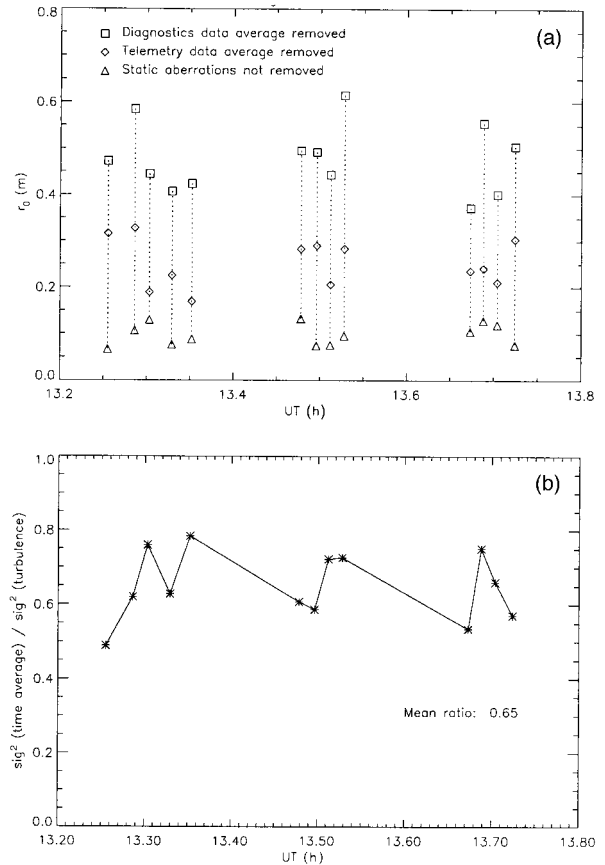


Fig. 14. (a) Values of  $r_0$  obtained from diagnostics data sets on 23 September 2002. The triangles show the results if no data conditioning is done, that is, if static aberrations are not removed. The squares show the results if the time average of a diagnostics data set is subtracted from this set. The diamonds, representing the most accurate estimates of  $r_0$ , are obtained if the averages of close-to-simultaneous telemetry data sets are subtracted. (b) We plot the ratio of the phase variances of the cases shown as squares and diamonds in (a). This quantity is the percentage of the turbulence strength that appears static in the 1.5-s data sets.

from these diagnostics sets. The necessity for this is demonstrated in Fig. 14, where we show the large differences between results if static aberrations are not subtracted (triangles), if the time average of the diagnostics data is subtracted (squares), or if the averages of close-to-simultaneous telemetry data sets are used to estimate the static aberrations (diamonds). In Fig. 14(b) we show the ratio of the phase variances between the cases shown as squares and diamonds in Fig. 14(a). Under the conditions of this night, on average two thirds of the turbulence strength appears static for 1.5-s data sets. If one wants to analyze diagnostics data, it is therefore necessary to have an independent estimate of the static aberrations, for example, from long telemetry data sets. However, the results of Figs. 11 and 13 show that even in that case the average of many sets of diagnostics data has to be taken to arrive at results that are representative for the current turbulence conditions.

We finally point out that the outer scale cannot be estimated from diagnostics data. The short sampling time of these data reduces the variances of low-order modes with respect to higher-order modes, which is the same effect as that of a small outer scale. Because it is not possible to separate the two effects, no outer scale measurements can be obtained from diagnostics data.

## 8. Conclusion

We have presented two different and independent methods that produce reliable results for atmospheric parameters from TT-loop-closed data with the two adaptive optics systems of the W. M. Keck Observatory, the analysis of DIM structure functions and the ZD of the wave-front phase. A large part of this paper is dedicated to a detailed description of the practical implementation of the methods. Of particular importance is the calibration of the WFSs of the AO systems, that is, primarily of the spot size on the WFS detector. Small changes of this spot size can cause significant errors in the resultant calibration and thus in the calculated quantities.

We have shown that both methods produce consistent results for both the atmospheric coherence length  $r_0$  and the outer scale of turbulence  $\mathcal{L}_0$  and that  $r_0$  values are in excellent agreement with results from long-exposure images. Values found for  $\mathcal{L}_0$  are mostly of the order of tens of meters, consistent with what has been found at many other sites.<sup>26</sup> We have also shown that telemetry data need to be taken at frame rates of 4 Hz or faster and that at least a few tens of seconds of data should be acquired so that the results can be considered representative for the given turbulence conditions.

We thank Aziz Ziad, Lothar Noethe, and Andrei Tokovinin for fruitful discussions of methods of atmospheric turbulence characterization and for their input concerning the research presented in this paper. Data presented herein were obtained at the W. M. Keck Observatory, which is operated as a scientific partnership among the California Institute of Technology, the University of California, and the National Aeronautics and Space Administration. The observatory was made possible by the generous financial support of the W. M. Keck Foundation. This research has been supported in part by the National Science Foundation Science and Technology Center for Adaptive Optics, managed by the University of California at Santa Cruz under cooperative agreement AST-9876783. The authors recognize and acknowledge the significant cultural role and reverence that the summit of Mauna Kea has always had within the indigenous Hawaiian community. We are most fortunate to have the opportunity to conduct observations from this mountain.

## References

1. L. M. Close, "Review of published galactic and solar system science: a bright future for adaptive optics science," in *Adaptive Optical Systems Technology*, P. L. Wizinowich, ed., Proc. SPIE **4007**, 758–772 (2000).

2. P. Wizinowich, D. S. Acton, C. Shelton, P. Stomski, J. Gathright, K. Ho, W. Lupton, K. Tsubota, O. Lai, C. Max, J. Brase, J. An, K. Avicola, S. Olivier, D. Gavel, B. Macintosh, A. Ghez, and J. Larkin, "First light adaptive optics images from the Keck II Telescope: a new era of high angular resolution imagery," *Publ. Astron. Soc. Pac.* **112**, 315–319 (2000).
3. M. Troy, R. G. Dekany, G. Brack, B. R. Oppenheimer, E. E. Bloemhof, T. Trinh, F. G. Dekens, F. Shi, T. L. Hayward, and B. Brandl, "Palomar adaptive optics project: status and performance," in *Adaptive Optical Systems Technology*, P. L. Wizinowich, ed., Proc. SPIE **4007**, 31–40 (2000).
4. D. Bonaccini, E. Prieto, P. Corporon, D. Le Mignant, P. Prado, R. Gredel, N. Hubin, and J. Christou, "Performance of the ESO AO system, Adonis, at La Silla 3.6 m telescope," in *Sol-Gel Optics IV*, B. S. Dunn, J. D. MacKenzie, E. J. Pope, H. K. Schmidt, and M. Yamane, eds., Proc. SPIE **3136**, 589–594 (1997).
5. A. Glindemann, S. Hippler, T. Berkefeld, and W. Hackenberg, "Adaptive optics on large telescopes," *Exp. Astron.* **10**, 5–47 (2000).
6. F. Rigaut, D. Salmon, R. Arsenault, J. Thomas, O. Lai, D. Rouan, J. P. Véran, P. Gigan, D. Crampton, J. M. Fletcher, J. Stilburn, C. Boyer, and P. Jagourel, "Performance of the Canada-France-Hawaii Telescope adaptive optics bonnette," *Publ. Astron. Soc. Pac.* **110**, 152–164 (1998).
7. P. L. Wizinowich, D. Le Mignant, P. J. Stomski, D. S. Acton, A. R. Contos, and C. Neyman, "Adaptive optics developments at Keck Observatory," in *Adaptive Optical System Technologies II*, P. L. Wizinowich and D. Bonaccini, eds., Proc. SPIE **4839**, 9–20 (2002).
8. P. Y. Madec, J. M. Conan, and G. Rousset, "Temporal characterization of atmospheric wavefront for adaptive optics," in *Progress in Telescope and Instrumentation Technologies*, M.-H. Ulrich, ed., Vol. 42 of ESO Proceedings (European Southern Observatory, Garching, Germany, 1992), p. 471.
9. E. Gendron and P. Léna, "Single layer atmospheric turbulence demonstrated by adaptive optics observations," *Astrophys. Space Sci.* **2**, 221–228 (1996).
10. B. L. Ellerbroek, D. J. Lee, and J. D. Barchers, "Analysis of atmospheric turbulence measurements obtained with the Starfire Optical Range 3.5-m telescope adaptive optical system," in *Adaptive Optics Systems and Technology*, R. K. Tyson and R. Q. Fugate, eds., Proc. SPIE **3762**, 212–224 (1999).
11. S. Harder and A. Chelli, "Estimating the point spread function of the adaptive optics system ADONIS using the wavefront sensor measurements," *Astron. Astrophys. Suppl. Ser.* **142**, 119–135 (2000).
12. M. Schöck and E. J. Spillar, "Method for a quantitative investigation of the frozen flow hypothesis," *J. Opt. Soc. Am. A* **17**, 1650–1658 (2000).
13. D. T. Gavel, C. E. Max, S. S. Olivier, B. J. Bauman, D. M. Pennington, B. A. Macintosh, J. Patience, C. G. Brown, P. M. Danforth, R. L. Hurd, E. L. Gates, S. A. Severson, and J. P. Lloyd, "Recent science and engineering results with the laser guide star adaptive optic system at Lick Observatory," in *Adaptive Optical System Technologies II*, P. L. Wizinowich, ed., Proc. SPIE **4839**, 354–359 (2002).
14. P. L. Wizinowich, D. S. Acton, T. Gregory, P. J. Stomski, J. R. An, K. Avicola, J. M. Brase, H. W. Friedman, D. T. Gavel, and C. E. Max, "Status of the W. M. Keck adaptive optics facility," in *Adaptive Optical System Technologies*, D. Bonaccini and R. K. Tyson, eds., Proc. SPIE **3353**, 568–578 (1998).
15. J. M. Brase, J. R. An, K. Avicola, B. V. Beeman, D. T. Gavel, R. L. Hurd, B. Johnston, H. E. Jones, T. C. Kuklo, C. E. Max, S. S. Olivier, K. E. Waltjen, and J. A. Watson, "Wavefront control system for the Keck telescope," in *Adaptive Optical System Technologies*, D. Bonaccini and R. K. Tyson, eds., Proc. SPIE **3353**, 517–521 (1998).

16. M. Sarazin and F. Roddier, "The ESO differential image motion monitor," *Astron. Astrophys.* **270**, 294–300 (1990).
17. F. Roddier, "The effects of atmospheric turbulence in optical astronomy," in *Progress in Optics*, E. Wolf, ed. (North-Holland, Amsterdam, 1981), Vol. 19, pp. 281–376.
18. A. Tokovinin, "From differential image motion to seeing," *Publ. Astron. Soc. Pac.* **114**, 1156–1166 (2002).
19. R. Conan, J. Borgnino, A. Ziad, and F. Martin, "Analytical solution for the covariance and for the decorrelation time of the angle of arrival of a wave front corrugated by atmospheric turbulence," *J. Opt. Soc. Am. A* **17**, 1807–1818 (2000).
20. G. A. Tyler, "Bandwidth considerations for tracking through turbulence with 8-m telescopes," *J. Opt. Soc. Am. A* **11**, 358–367 (1994).
21. M. Schöck, D. Le Mignant, G. A. Chanan, and P. L. Wizinowich, "Atmospheric turbulence characterization with the Keck adaptive optics systems," in *Adaptive Optical System Technologies II*, P. L. Wizinowich and D. Bonaccini, eds., Proc. SPIE **4839**, 813–824 (2002).
22. R. J. Noll, "Zernike polynomials and atmospheric turbulence," *J. Opt. Soc. Am.* **66**, 207–211 (1976).
23. D. M. Winker, "Effect of a finite outer scale on the Zernike decomposition of atmospheric optical turbulence," *J. Opt. Soc. Am. A* **8**, 1568–1573 (1991).
24. W. H. Southwell, "Wave-front estimation from wave-front slope measurements," *J. Opt. Soc. Am.* **70**, 998–1006 (1980).
25. W. H. Press, S. A. Teukolsky, W. T. Vetterling, and B. P. Flannery, *Numerical Recipes in C*. 2nd ed. (Cambridge U. Press, Cambridge, England, 1992).
26. A. Ziad, R. Conan, A. Tokovinin, F. Martin, and J. Borgnino, "From the grating scale monitor to the generalized seeing monitor," *Appl. Opt.* **39**, 5415–5425 (2000).